

# One-Dimensional van der Waals Heterostructures as Efficient Metal-Free Oxygen Electrocatalysts

Chang Liu,<sup>1</sup> Fei Liu,<sup>1</sup> Hao Li,<sup>1</sup> Junsheng Chen, Jingyuan Fei, Zixun Yu, Ziwen Yuan, Chaojun Wang, Huiling Zheng, Zongwen Liu, Meiyong Xu, Graeme Henkelman,\* Li Wei,\* and Yuan Chen\*



Cite This: *ACS Nano* 2021, 15, 3309–3319



Read Online

ACCESS |



Metrics & More

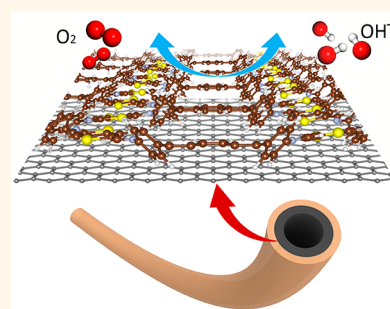


Article Recommendations



Supporting Information

**ABSTRACT:** Two-dimensional covalent organic frameworks (2D-COFs) may serve as an emerging family of catalysts with well-defined atomic structures. However, the severe stacking of 2D nanosheets and large intrinsic bandgaps significantly impair their catalytic performance. Here, we report coaxial one-dimensional van der Waals heterostructures (1D vdWHs) comprised of a carbon nanotube (CNT) core and a thickness tunable thienothiophene-pyrene COF shell using a solution-based *in situ* wrapping method. Density functional theory calculations and *operando* and *ex situ* spectroscopic analysis indicate that carbon–sulfur regions in thienothiophene groups in the COF serve as an active catalytic site for oxygen reduction and evolution reactions. The coaxial structure enables *n*-doping from the CNT core to the COF shell, which is controllable by varying COF shell thickness. The charge transfer from CNTs lowers COF's bandgap and work function, which reduces the charge transfer barrier between the active catalytic sites and adsorbed oxygen intermediates, resulting in dramatically enhanced catalytic activity. The 1D vdWHs were applied as a bifunctional oxygen electrocatalyst in rechargeable zinc–air batteries, delivering a high specific capacity of 696 mAh g<sub>Zn</sub><sup>-1</sup> under a high current density of 40 mA cm<sup>-2</sup> and excellent cycling stability. The 1D vdWHs based on the coaxial structure of 2D COF wrapped around CNT cores may be further used as versatile building units to create multidimensional vdWHs for exploring fundamental physics and chemistry as well as practical applications in electrochemistry, electronics, photonics, and beyond.



**KEYWORDS:** covalent organic framework, carbon nanotube, van der Waals heterostructure, oxygen redox reaction, zinc-air battery

Two-dimensional covalent organic frameworks (2D-COFs) are planar nanosheets in a periodic lattice, assembled from covalently bonded small molecules.<sup>1–8</sup> They possess several outstanding properties for enabling high-activity catalysts, for example, a large specific surface area, tunable porosity, and excellent thermal and chemical stability. More importantly, versatile molecular building blocks of 2D-COFs may offer well-defined and structurally tunable catalytic active sites with atomic precision.<sup>9</sup> Recently, 2D-COFs have been explored as an emerging family of electrocatalysts for the oxygen reduction reaction (ORR) and oxygen evolution reaction (OER).<sup>10–17</sup> The ORR and OER processes involve the transfer of four electrons. Their sluggish kinetics result in the unsatisfactory performance of many energy storage and conversion devices, such as zinc–air batteries (ZABs), fuel cells, and water electrolyzers. Precious metal based electrocatalysts, including platinum (Pt), ruthenium (Ru), and iridium (Ir), have high catalytic activity for ORR and OER; however, their high cost and low abundance on the earth limit their widespread applications. On the contrary, 2D-COFs can

be synthesized at a low cost without using precious metals and may serve as efficient metal-free electrocatalysts for these electrochemical reactions.<sup>18,19</sup> However, there are two challenges for these materials to serve as efficient electrocatalysts. First, abundant out-of-plane  $\pi$ -electrons on 2D-COFs cause spontaneous stacking of 2D nanosheets, resulting in thick COF laminates, blocking the access to surface-active catalytic sites and sabotaging mass transfer of electrolytes, reactants, and products.<sup>7,8</sup> Second, their conjugated  $\pi$ -electron skeletons may open few-eV intrinsic bandgaps, impairing efficient electron transfer.<sup>20,21</sup>

**Received:** December 8, 2020

**Accepted:** January 21, 2021

**Published:** January 25, 2021



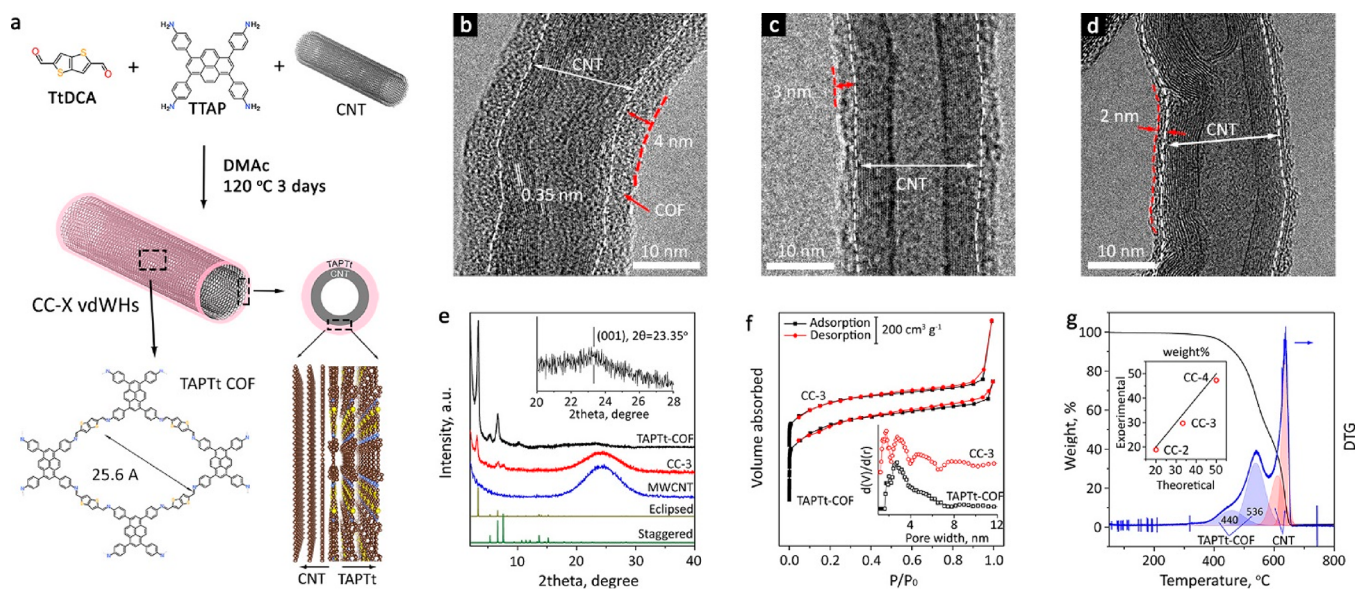


**Figure 1.** (a) Schematic illustration of the synthesis of 1D vdWHs (CC-X). (b–d) TEM images of (b) CC-4, (c) CC-3, and (d) CC-2. (e) XRD patterns (inset: magnified (001) region of TAPTt-COF). (f)  $N_2$  physisorption isotherms of TAPTt-COF and CC-3 (inset: pore size distributions). (g) TGA and DTG profiles of CC-3 (inset: weight fraction of COF in CC-X).

Creating nanohybrids of 2D-COFs and carbon nanotubes (CNTs) may overcome the above challenges because CNTs can serve as spacers to prevent the stacking of 2D-COF and provide fast electron transfer paths.<sup>22–26</sup> Along these lines, CNTs have been used to synthesize composites with 2D graphene or  $g-C_3N_4$  nanosheets.<sup>27–31</sup> Further, intermolecular charge transfer may occur between CNTs and their surface adsorbates, which have been explored to modulate the adsorbates' catalytic activity.<sup>10,31–34</sup> Composites can be formed by metallic, ionic, or covalent bonds. However, precise control of these strong chemical bonds is difficult, and the formation of these strong chemical bonds can also significantly interrupt the intrinsic properties of constituting components. Alternatively, 2D crystals have been assembled into van der Waals heterostructures (vdWHs) by stacking multiple 2D layers on top of each other, representing a different way to form crystals.<sup>35,36</sup> In a recent study, 1D vdWHs were synthesized by growing boron nitride or molybdenum disulfide crystals on CNTs.<sup>37</sup> We envision that coaxial 1D vdWHs can be synthesized *via*  $\pi$ -electron interactions between 2D-COF and CNTs *via* bottom-up synthesis, in which 2D-COFs may serve as the shell, while CNTs are the core. The interactions between 2D-COFs and CNTs in such 1D vdWHs may enable high-performance electrocatalysts.

Herein, we report the design and synthesis of 1D vdWHs comprised of 2D-COFs and CNTs. We used an *in situ* wrapping method to grow and assemble a catalytically active thienothiophene-containing 2D-COF shell around a catalytic inert multiwalled CNT (MWCNT) core. This method allows the precise tuning of the thickness of the COF shell in the nanometer scale, leading to discovering the shell thickness-dependent high electrocatalytic activity for both ORR and OER. Density functional theory (DFT) calculations, diffusive reflectance ultraviolet–visible spectroscopy (UV–vis DRS), and ultraviolet photoelectron spectroscopy (UPS) were applied to understand electronic interactions in the 1D vdWHs, revealing significant *n*-doping from CNTs to COF shells. Further theoretical calculations and *operando* Fourier transformed infrared spectroscopy (FTIR) studies were used

to identify the specific catalytic active site. The practical application of the 1D vdWH as a highly efficient bifunctional oxygen electrocatalyst was also demonstrated in high-performance rechargeable ZABs.

## RESULTS AND DISCUSSION

**Synthesis and Physicochemical Characterization.** As illustrated in Figure 1a, a thienothiophene-containing molecule, thieno[3,2-*b*]thiophene-2,5-dicarboxaldehyde (TtDCA), was used to construct a 2D-COF with 4,4',4'',4'''-(pyrene-1,3,6,8-tetrayl)tetraaniline (TTAP). We chose TtDCA because the two symmetric S-pentacyclic domains in its thienothiophene group can readily mimic the S–C structures in S-doped carbon materials, which can act as bifunctional catalytic sites for ORR and OER.<sup>38</sup> The Schiff-base condensation between TtDCA and TTAP in the presence of CNTs in *N,N*-dimethylacetamide (DMAc) produced 1D coaxial vdWHs with COF shell of a tunable thickness, as described in the Methods. The thickness of the COF shell can be controlled by tuning the mass ratio between CNTs and COF precursors ( $m_{\text{CNT}}/m_{\text{precursors}} = 1, 2, \text{ or } 4$ ). The resulting 1D vdWHs are denoted as CC-X, where X refers to the thickness of the COF shell in nanometers measured by transmission electron microscope (TEM).

The successful formation of TAPTt-COF was first examined by Fourier transform infrared spectroscopy (FTIR, Figure S1). The peak at  $1658\text{ cm}^{-1}$  can be assigned to imine ( $-\text{C}=\text{N}-$ ) bonds in the framework. The  $^{13}\text{C}$  solid-state nuclear magnetic resonance (ssNMR) spectrum exhibits several peaks, which can be assigned to the predicted atomic structure of the TAPTt COF (Figure S2). The formation of the imine bond can be further confirmed by the peak at a chemical shift of  $\sim 152$  ppm. An AFM image and the corresponding height profiles of pristine TAPTt-COF (Figure S3) exhibits a large nanosheet ( $\sim 2 \times 4\ \mu\text{m}^2$ ) with a thickness of about 1.5 nm (4 atomic layers), confirming its 2D structure. Small-diameter multiwalled CNTs (MWCNTs) used in this study have smooth and clean surfaces (see TEM images in Figure S4). In comparison,

TEM images in Figure 1b–d show that seamless COF shells with varied thicknesses are formed on CNTs. The thickness of the COF shells can be precisely controlled at a nanometer-scale precision. Figure 1b–d display the thickness of COF shells is 4.2, 3.0, and 1.9 nm in the 1D vdWHs synthesized using COF precursors to CNTs at the mass ratio ranging from 4, 2, to 1 (Table 1).

**Table 1. Physiochemical Properties of TAPTt-COF, CNTs, and CC-X 1D vdWHs**

samples	$m_{\text{CNT}}/$ $m_{\text{precursors}}$	thickness of COF shell <sup>a</sup> (nm)	SSA ( $\text{m}^2 \text{g}^{-1}$ )	COF mass loading <sup>b</sup> (%)
CC-4	1	4.2 ± 0.5	629	47.3
CC-3	2	3.0 ± 0.4	436	29.7
CC-2	4	1.9 ± 0.2	296	18.9
TAPTt			1059	
MWCNT			112	

<sup>a</sup>The thickness was measured by TEM. <sup>b</sup>The mass loading was determined by DTG.

Strong  $\pi$ – $\pi$  interactions occur between CNTs and pyrene groups in TTAP,<sup>39</sup> and we expect that such interactions play a critical role in guiding the formation of the 1D core–shell structured vdWHs. Without the presence of CNTs, pristine TAPTt-COF self-assembles into microspheres with a diameter of about 2–3  $\mu\text{m}$ , as shown in the scanning electron microscope (SEM) images in Figure S5. These COF microspheres contain well-aligned nanochannels around 2.5 nm wide, as confirmed by TEM observation shown in Figure S6, consistent with a molecular model of this type of COF. In contrast, only tubular structures are observed in the SEM images of CC-X vdWHs (Figure S7). Although the COF shells' morphology changes significantly by the CNT cores, they retain their chemical characteristics. Figure S8 shows that their FTIR spectra are similar to that of pristine TAPTt-COF. Their XPS survey scans (Figure S9) and the corresponding high-resolution X-ray photoelectron spectroscopy (XPS) spectra of C1s, N1s, and S2p are virtually identical to that of pristine TAPTt-COF (Figure S10–S12). Figure S13 shows that O exists in chemisorbed water on CNTs and CC-X vdWHs with a low O content (<3 atom %). It should be noted that the XPS results indicate a low concentration of oxygenated functional groups, which were considered as active catalytic sites in a previous study.<sup>40</sup>

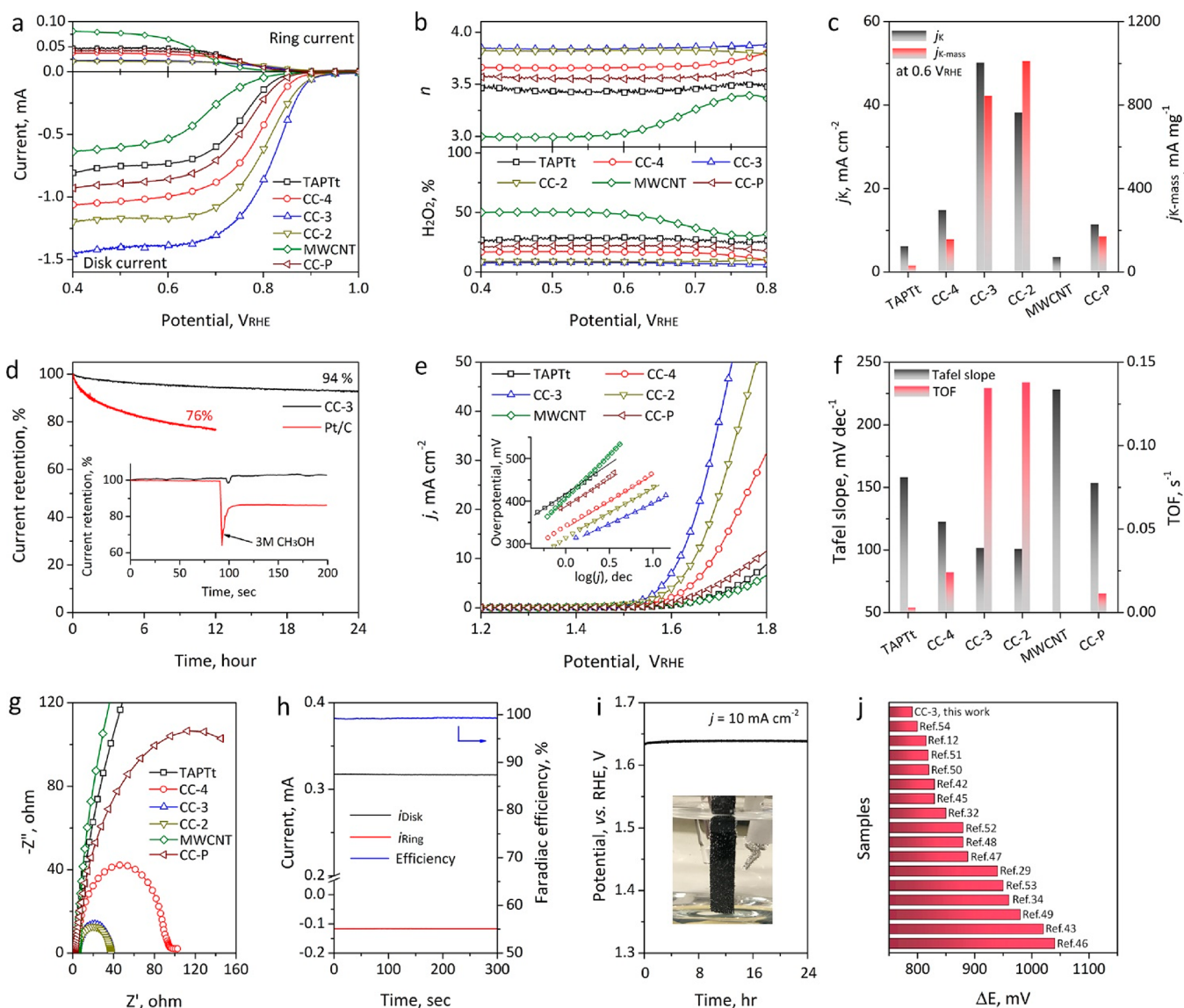
Powder X-ray diffraction (XRD) patterns of pristine TAPTt-COF, CC-3, and CNTs are presented in Figure 1e. TAPTt-COF shows an XRD pattern consistent with its simulated eclipsed stacking model (orthorhombic,  $a = 33.0 \text{ \AA}$ ,  $b = 44.6 \text{ \AA}$ ,  $c = 6.5 \text{ \AA}$ ,  $\alpha = \beta = \gamma = 90^\circ$ , Figure S14). The distinctive peaks at  $2\theta = 3.38^\circ$ ,  $5.35^\circ$ , and  $6.67^\circ$ , which can be assigned to the (100), (200), and (220) planes, respectively. There is an interlayer d-spacing of  $\sim 0.38 \text{ nm}$  from the most intense (001) reflection at a  $2\theta$  of  $23.35^\circ$  (inset of Figure 1e, Cu  $K\alpha$ ,  $\lambda = 1.5406 \text{ \AA}$ ). In comparison, the CC-3 vdWH displays the features of TAPTt-COF and a broad peak from the (001) diffraction of CNTs at  $\sim 25^\circ$ . A different peak emerges at  $2\theta = 7.59^\circ$ , assigned to the (111) reflection of TAPTt COF in a staggered stacking model (Figure S15). We assume the highly flexible imine bond in the TAPTt structure could allow the bending of the COF shell to the surface curvature of the carbon nanotube core.<sup>41</sup>  $\text{N}_2$  physisorption isotherms and corresponding pore size distribution profiles are displayed in

Figure 1f and Figure S16. TAPTt-COF exhibits a large specific surface area of  $1059 \text{ m}^2 \text{ g}^{-1}$  with abundant mesopores at  $\sim 2.5 \text{ nm}$ . The specific surface area of CC-X vdWHs is listed in Table 1, showing a decreasing trend from 629 to  $296 \text{ m}^2 \text{ g}^{-1}$  with reducing COF shell thickness. Their pore size distribution profiles (Figure S16) show a different pore at  $\sim 1.6 \text{ nm}$ , which can be assigned to such pores in TAPTt COF packed in the staggered stacking model (Figure S15).

The mass loading of TAPTt-COF in CC-X vdWHs was determined by thermogravimetric analysis (TGA) and differentiated thermogravimetric analysis (DTG). Figure 1g shows the representative TGA and DTG profiles of CC-3. The DTG profile's deconvolution reveals two distinctive groups of peaks at 440 and  $536^\circ \text{C}$  and  $>600^\circ \text{C}$ , which can be attributed to the thermal decomposition of TAPTt-COF and CNTs (Figure S17), respectively. The mass loading of COF in CC-3 is 29.7 wt % (Table 1), similar to the mass ratio between CNT and COF precursors (2:1). The mass loadings of COF in CC-4 and CC-2 exhibit the same agreement (inset of Figure 1g and Figure S17). Overall, different physiochemical characterization results confirm that our *in situ* wrapping method can precisely control COF shells' thickness in the resulting 1D core–shell structured vdWHs.

**Electrocatalytic Properties.** The electrocatalytic performances of CC-X vdWHs and several commercial catalysts as references were evaluated in  $\text{O}_2$ -saturated 0.1 M KOH electrolyte. Figure 2a shows their ORR linear sweep voltammetry (LSV) curves collected on rotary ring-disk electrode (RRDE). Their half-wave potentials ( $E_{1/2}$ ) are listed in Table 2 for comparison. There is a clear trend that the electrocatalytic activity of CC-X vdWHs depends on their COF shells' thickness. CC-3 exhibits the highest activity for ORR activity among the three vdWHs with the highest  $E_{1/2}$  of 0.828 V (*vs* reversible hydrogen electrode (RHE)), which is also much higher than that of pristine TAPTt-COF at 0.741 V, CNTs at 0.698 V, and a physical mixture of TAPTt-COF and CNT at 0.761 V (at a mass ratio of 1:2, denoted as CC-P, see the Methods for details). The electron transfer number ( $n$ ) and the selectivity to  $\text{H}_2\text{O}_2$  selectivity are calculated and compared in Figure 2b. CC-X vdWHs follow a stable  $4e^-$  ORR pathway in the tested potential window. The  $n$  of CC-3 is  $\sim 3.86$ , close to that of 20 wt % Pt/C at 3.95 (Figure S18). Further, Koutecky–Levich (K–L) plots of different samples are compared to envisage their kinetic properties (Figure S19). The electron-transfer numbers were also determined from the K–L plots at 0.7  $V_{\text{RHE}}$ , and the results are listed in Table 2.

The kinetic current densities ( $j_{\text{K}}$ ) at 0.6  $V_{\text{RHE}}$  of different samples are compared in Figure 2c. The  $j_{\text{K}}$  of CC-3 ( $50.17 \text{ mA cm}^{-2}$ ) and CC-2 ( $38.19 \text{ mA cm}^{-2}$ ) are much higher than that of CC-1 ( $14.86 \text{ mA cm}^{-2}$ ) and CC-P ( $9.37 \text{ mA cm}^{-2}$ ). Besides, the  $j_{\text{K}}$  of CC-3 is also higher than that of 20 wt % Pt/C ( $46.57 \text{ mA cm}^{-2}$ ). Assuming TAPTt COF or Pt as the active catalytic component, the mass-normalized kinetic current density ( $j_{\text{K-mass}}$ ) was calculated and listed in Table 2. Figure 2c shows that the  $j_{\text{K-mass}}$  decreases with an increase in the COF shell thickness. CC-2 has the largest  $j_{\text{K-mass}}$  of  $1.01 \text{ A mg}^{-1}$ , which is  $\sim 16\%$  higher than that of CC-3 ( $0.84 \text{ A mg}^{-1}$ ) and over 30 times larger than that of TAPTt-COF ( $0.03 \text{ A mg}^{-1}$ ). However, because the mass loading of COF in CC-2 is lower than that in CC-3, CC-3 exhibits better overall catalytic performance for ORR. The stability test results shown in Figure 2d indicate that CC-3 has better stability than Pt/C. It retains 94% of its initial current density after the 24-h



**Figure 2.** Electrochemical performance. (a) ORR RRDE-LSV curves and (b) calculated  $n$  and  $\text{H}_2\text{O}_2$  %. (c) Comparison of  $n$  and  $j_K$  at  $0.6 V_{\text{RHE}}$ . (d) ORR stability and methanol tolerance test (inset) of CC-3. (e) OER-LSV curves and Tafel plots (inset). (f) Comparison of Tafel slopes and TOFs. (g) OER EIS Nyquist plots. (h) Faradaic efficiency and (i) OER stability of CC-3. (j) Comparison of recently reported bifunctional oxygen electrocatalysts with CC-3.

**Table 2.** Electrochemical Performances for ORR and OER of Different Catalysts

	ORR performance					OER performance				
	$E_{1/2}$ (V)	$n^a$	$n^b$	$j_K^b$ ( $\text{mA cm}^{-2}$ )	$j_{K\text{-mass}}^b$ ( $\text{A mg}^{-1}$ )	$\eta_{10}$ (mV)	Tafel slope ( $\text{mV dec}^{-1}$ )	TOF <sup>c</sup> ( $\text{s}^{-1}$ )	$R_{CT}^d$ (ohm)	
CC-4	0.771	3.62	3.64	14.86	0.16	457	122	0.0242	98.6	
CC-3	0.828	3.86	3.89	50.17	0.84	389	101	0.134	36.2	
CC-2	0.799	3.90	3.91	38.19	1.01	409	100	0.138	35.4	
TAPTt	0.741	3.45	3.42	6.21	0.03	605	158	0.00288	486.9	
MWCNT	0.698	3.21	3.14	3.60		751	228		551.2	
CC-P	0.761	3.54	3.57	8.37	0.13	578	153	0.0114	223.7	
Pt/C	0.865	3.95	3.96	46.57	1.16					

<sup>a</sup>Determined from RRDE tests at  $0.7 V_{\text{RHE}}$ . <sup>b</sup>Calculated from K-L plots at  $0.7 V_{\text{RHE}}$ . <sup>c</sup>Calculated at  $\eta = 400$  mV. <sup>d</sup>Obtained at  $\eta = 350$  mV.

chronoamperometric test at  $0.4 V_{\text{RHE}}$ . In comparison, Pt/C lost 24% of its initial current density in 12 h. CC-S also exhibits good methanol tolerance (inset of Figure 2d).

The OER performance was also assessed in 0.1 M KOH electrolyte. Figure 2e displays the LSV curves of different

samples. TAPTt-COF, CNTs, and CC-P show negligible OER catalytic activity. In contrast, CC-X vdWHs have much higher activities (Table 2). Among the three samples, CC-3 demonstrates the best catalytic performance with the lowest overpotential ( $\eta_{10}$ ) of 389 mV to achieve the current density

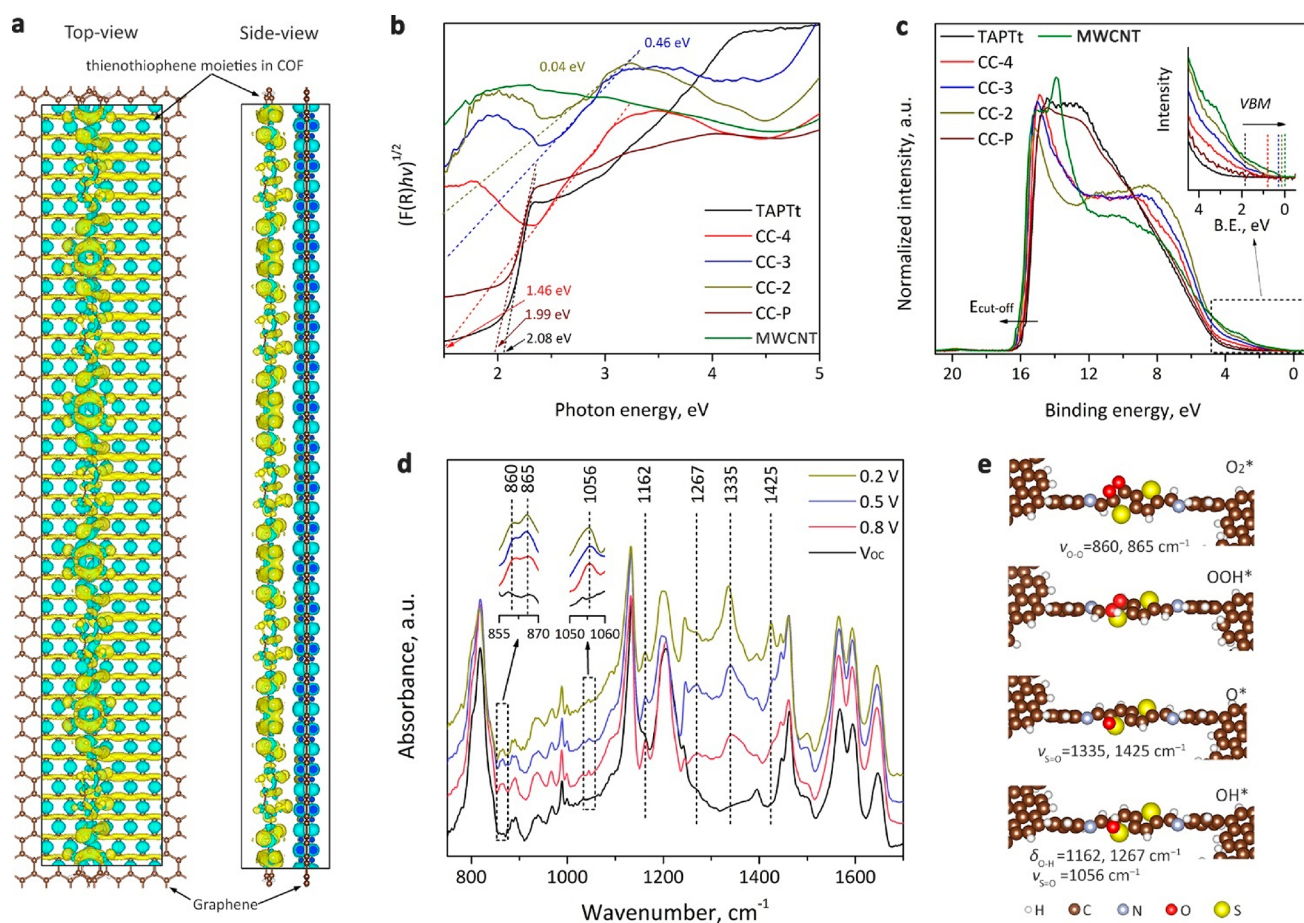


**Figure 3.** Mechanism investigation by theoretical calculations and spectroscopic studies. (a) Calculated charge density difference profiles of CC-X vdWHs. (b) DRS and (c) UPS spectra (inset: spectra near the Fermi level). (d) *Operando* FTIR spectra of CC-3 in O<sub>2</sub> saturated 0.1 M KOH electrolyte under different ORR potentials. (e) DFT-optimized intermediate adsorption geometries and the corresponding experimental IR band assignments.

(j) of 10 mA cm<sup>-2</sup>. The inset of Figure 2e shows Tafel plots of different samples, and their Tafel slopes are compared in Figure 2f. CC-3 and CC-2 have comparable Tafel slopes of 101 and 100 mV dec<sup>-1</sup>, respectively, indicating similar OER kinetics.

The current densities of different samples were further normalized according to their electrochemically active surface area (ECSA, measured by the cyclic voltammetry (CV) scanning method, Figure S20). The  $j_{\text{ECSA}}$  (Figure S21) suggests a similar performance trend as that in Figure 2d, except that the current density difference between CC-3 and CC-2 is reduced. Assuming that the active catalytic sites are on TAPTt-COF, we calculated the turnover frequency (TOF) of our different samples, as shown in Figure S22 (see the Methods for details). The TOFs at a  $\eta = 400$  mV are compared in Figure 2f. The TOF of CC-2 at 0.138 s<sup>-1</sup> is slightly higher than that of CC-3 at 0.134 s<sup>-1</sup>, suggesting its higher intrinsic activity, which is consistent with the results of their catalytic activity for ORR.

Electrochemical impedance spectroscopy (EIS) was used to determine the charge transfer resistance ( $R_{\text{ct}}$ ). A Nyquist plot is shown in Figure 2g, and the values of  $R_{\text{c}}$  determined at  $\eta = 350$  mV are listed in Table 2.  $R_{\text{ct}}$  depends on the thickness of the COF shells. Figure 2h shows that CC-3 delivers a near-unity Faradaic efficiency (99.2%), as determined by an RRDE method.<sup>42</sup> It also displays excellent stability with less than 4%

overpotential increment in the 24-h chronopotentiometric stability test under 10 mA cm<sup>-2</sup> (Figure 2i). The inset of Figure 2i shows a photo of oxygen bubbles on a CC-3 electrode.

We further compared ORR  $E_{1/2}$  and OER  $\eta_{10}$  of CC-3 with recently reported metal-free and carbon-based bifunctional oxygen electrocatalysts (listed in Table S1). The potential difference ( $\Delta E$ ) between the  $E_{1/2}$  and  $\eta_{10}$  collected in 0.1 M KOH electrolyte is calculated to compare their bifunctional catalytic activity. As displayed in Figure 2j, CC-3 shows the smallest  $\Delta E$  of 791 mV. Alternatively, we also compiled a catalytic activity atlas by plotting ORR  $E_{1/2}$  against OER  $\eta_{10}$ . As shown in Figure S23, CC-3 is located at the bottom-left, suggesting one of the best catalytic performances among recently reported metal-free carbon electrocatalysts.<sup>12,29,32,43–55</sup>

**Origin of Catalytic Activity.** The electrocatalytic performance test results above suggest that the ORR and OER activity of 1D CC-X vdWHs depends strongly on the thickness of COF shells. We combined theoretical and spectroscopic studies to understand this dependence and explore the origin of their superior catalytic activity. We first analyzed electronic interactions by DFT calculations. The atomic geometry optimized CC-X vdWHs was modeled as thienothiophene moieties sitting on a graphene substrate. Figure 3a shows that the graphene substrate (electron-deficient, blue color) injects

abundant delocalized electrons to thienothiophene moieties (electron-rich, yellow color), resulting in the *n*-doping effect to the COF shell. The delocalized electrons, which can be treated as excessive carriers, can change the COF shell electronic properties and, consequently, its electrochemical activity.<sup>56</sup>

We hypothesize that the COF shell's excessive carriers should follow the well-established carrier continuity equation, which describes the decaying of excessive carriers in semiconductors as schematically illustrated in Figure S24.<sup>57</sup> To prove our hypothesis, we compared the near-surface carrier density of CC-X vdWHs and pristine TAPTt-COF by applying the Mott–Schottky analysis.<sup>58</sup> As shown in Figure S25, their Mott–Schottky plots (reciprocal square root of capacitance vs potential) all exhibit positive slopes, confirming the *n*-doping in the CC-X vdWHs.<sup>59</sup> The value of this slope is inversely proportional to the near-surface carrier density. The smallest slope of CC-2 indicates its highest carrier density among the CC-X vdWHs (Table 2). We further plotted the reciprocal of the Mott–Schottky slopes as a function of the COF shell thickness in CC-X vdWHs in Figure S26. The fast decaying trajectory can be well fitted to the solution of carrier continuity equation at steady state.<sup>57</sup> Thus, the COF thickness-dependent catalytic activity can be explained by the weakened electronic interaction between COF and CNT when the COF-shell thickness increases.

We further probed the *n*-doping effects in CC-X vdWHs by measuring their indirect bandgap using UV–vis DRS and near-surface work function ( $\Phi$ ) using UPS. Figure 3b shows that the bandgap of CC-X vdWHs decreases with the reduction of the COF shell thickness. TAPTt-COF has a bandgap of 2.08 eV, and CC-4, CC-3, and CC-2 have a bandgap of 1.58, 0.46, and 0.04 eV, respectively, approaching the bandgap of CNTs (0 eV, Table 3). Notably, the physically mixed CC-P has a

**Table 3. Electronic Properties of TAPTt COF, CNT, and CC-X vdWHs**

sample	bandgap (eV)	$\Phi$ (eV)	M–S slope ( $\times 10^8 \text{F}^{-2} \text{V}^{-1}$ )
TAPTt	2.08	5.47	1.29
CC-4	1.58	5.21	1.11
CC-3	0.46	4.99	0.79
CC-2	0.04	4.86	0.68
CC-P	1.99	5.41	1.18
CNT	~0	4.76	

bandgap of 1.99 eV, similar to that of TAPTt-COF, indicating that the bandgap modulation by CNTs is only possible when there are strong interactions between COF shells and CNTs. Further, the change of  $\Phi$  measured by UPS confirms the same trend (Table 3). USP spectra in Figure 3c show that the valence band maximum (VBM) upshift closer to the Fermi level in CC-X vdWHs with thinner COF shells as a result of higher delocalized electron density.

Based on the above results, we propose that the superior catalytic activity of CC-X vdWHs is related to the *n*-type electronic interaction between CNTs and COF shells. The *n*-doping lowers COF shells' bandgap and work function, leading to a reduced charge transfer barrier between COF shells and adsorbed oxygen intermediates.<sup>60</sup> Further, CC-2, with the thinnest COF shell, experiences the most substantial *n*-doping, thus exhibiting the highest catalytic activity for ORR and OER. However, CC-3 contains a higher mass ratio of COF, which translates into a significantly increased active site number and

better catalytic performance. Overall, CC-3 was identified as the optimal catalyst among the three CC-X vdWHs.

We further carried out theoretical calculations and spectroscopic studies to confirm the above-proposed origin of catalytic activity and elucidate the active catalytic center for oxygen redox reactions. Using the elementary steps and parameters proposed for ORR in previous studies,<sup>61,62</sup> we calculated the free energy diagram of ORR intermediates adsorbed on possible active sites of TAPTt COF. All atoms in the proposed model were allowed to relax. DFT results (Figure S27) show that the C–S region on the thienothiophene moiety is the only possible active site. The initial O<sub>2</sub> adsorption preferentially takes place at a C atom neighboring an S atom in the thienothiophene ring. After accepting a proton–electron pair, the OOH\* intermediate diffuses to the S atom and proceeds along the dissociative ORR pathway. Figure S28 shows that all other atoms are either inert for the initial O<sub>2</sub> adsorption or have weak adsorbate binding properties, ruling out their possibility as active sites.

Next, we utilized *operando* FTIR to verify the proposed active catalytic center on CC-3 during ORR. Figure 3d shows the *operando* FTIR spectra collected under open circuit potential ( $V_{OC}$ ) and different ORR potentials. The IR bands associated with the structure of TAPTt-COF are mostly unchanged, confirming its excellent electrochemical stability. When different ORR potentials were applied, several different features emerge, which are associated with varying intermediates of reaction, as displayed in Figure 3e. The peaks at 860 and 865 cm<sup>-1</sup> can be assigned to the O–O stretching ( $\nu_{O-O}$ ) in O<sub>2</sub>\* or OOH\* intermediates.<sup>63</sup> The S–O stretching ( $\nu_{S-O}$ ) peak at 1056 cm<sup>-1</sup> is close to our DFT-calculated frequency of 1066 cm<sup>-1</sup>. The O–H bending in S–O–H ( $\delta_{O-H}$ ) at 1162 and 1267 cm<sup>-1</sup> and the S=O stretching mode ( $\nu_{S=O}$ ) at 1335 and 1425 cm<sup>-1</sup> originate from intermediates formed along the dissociative ORR pathway. Further, the intensity of these S–O peaks increases under lower applied potentials, which is consistent with the reaction pathway determined from our DFT calculations.<sup>64</sup> Thus, both theoretical calculations and spectroscopic studies confirm that the predesignated C–S region on the thienothiophene moiety of TAPTt COF is the active catalytic center for oxygen redox reactions.

**Application in ZABs.** We further demonstrated the application of CC-3 as an efficient bifunctional O<sub>2</sub> electrocatalyst to enable high-performance rechargeable ZABs. The details of battery assembly are described in the Methods. Figure S29 shows that the CC-3 ZAB has an open circuit potential of 1.477 V, which is comparable to 1.489 V of the ZAB assembled using commercial Pt/C and IrO<sub>x</sub>/C catalysts (denoted as Pt–Ir/C). Figure 4a shows galvanodynamic charge/discharge profiles of two ZABs. The CC-3 ZAB delivers a maximum power density of 85 mW cm<sup>-2</sup>, which is 21% higher than that of the Pt–Ir/C ZAB (74 mW cm<sup>-2</sup>). Under the discharging current density of 10 mA cm<sup>-2</sup>, the capacity of the CC-3 ZAB is 714 mAh g<sub>Zn</sub><sup>-1</sup>, comparable to 712 mAh g<sub>Zn</sub><sup>-1</sup> of the Pt–Ir/C ZAB (Figure 4b). Under the high discharging current density of 40 mA cm<sup>-2</sup>, the CC-3 ZAB outperforms the Pt–Ir/C ZAB (696 vs. 684 mAh g<sub>Zn</sub><sup>-1</sup>, see the inset of Figure 4b).

The ZAB cycling performance was evaluated by 120 discharging/charging cycles ( $j = 10 \text{ mA cm}^{-2}$ , charge/discharge capacity is 5 mAh cm<sup>-2</sup> per cycle, Figure 4c). Both ZABs show similar performance at the first cycle with a

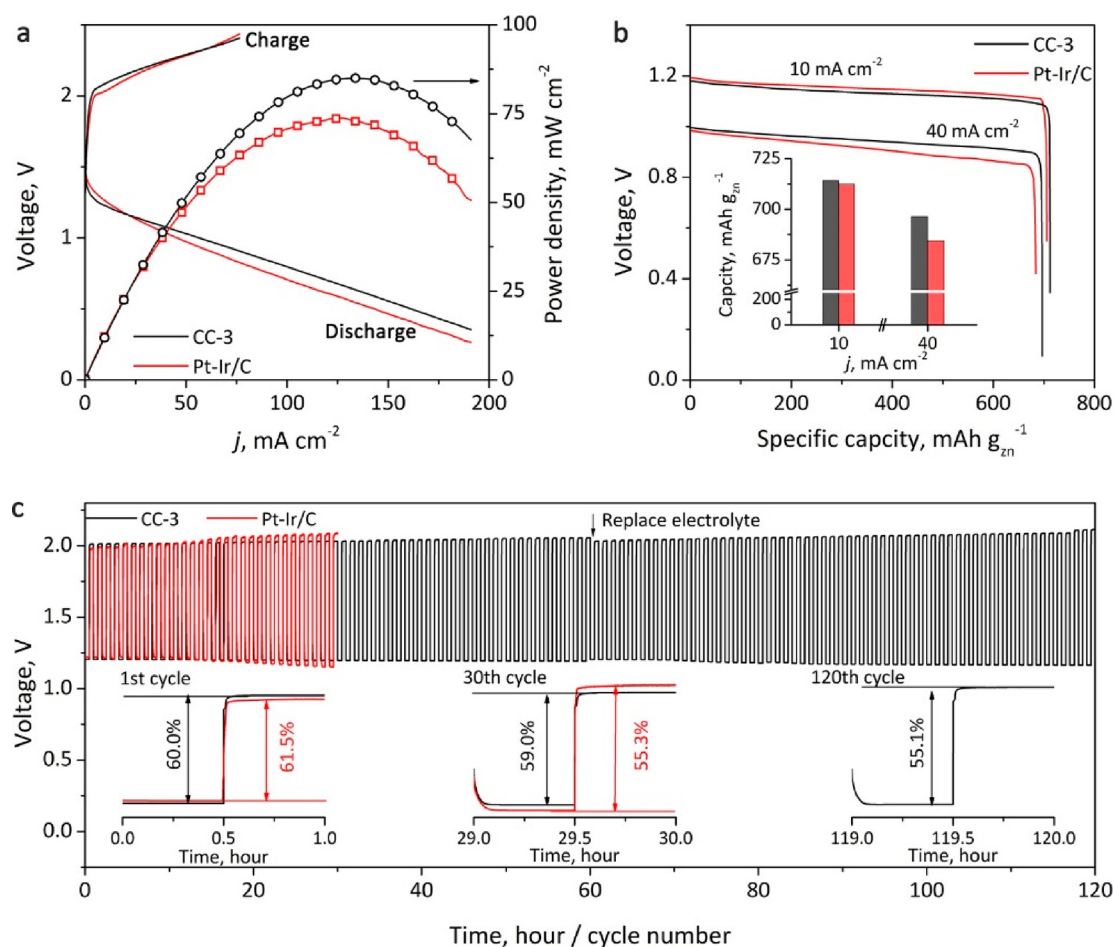


**Figure 4.** Performance of rechargeable zinc-air batteries assembled using CC-3 and Pt-Ir/C oxygen catalysts. (a) Galvanodynamic charge/discharge profiles and power density and (b) galvanostatic discharge curves. The inset shows the battery capacity under different discharge current densities. (c) Cycling profiles. The insets show cycling performances at 1st, 30th, and 120th cycles.

comparable round-trip efficiency of 60.0 and 61.5%, respectively (see the inset on the left in Figure 4c). After 30 cycles, the efficiency of the CC-3 ZAB declines slightly to 59.0%, while that of the Pt-Ir/C ZAB quickly drops to 55.3%. After 120 cycles, the CC-3 ZAB still retains a high efficiency of 55.1%. We also recorded *ex situ* XPS spectra of CC-3 after the 120-cycle rechargeability test. Figure S30 shows minor changes in N1s spectra, indicating the high electrochemical stability of imine bonds in TAPTt COF. In contrast, C1s, O1s, and S2p spectra exhibit substantial changes. Intensified C–O and C=O features are found in the deconvoluted C 1s spectrum. The O1s peak also shifts to the lower binding energy of 531.6 eV, which can be attributed to C–O and S–O chemical bonds' formation. A different peak emerged in the S2p spectrum at 168.8 eV, which can be assigned to S–O chemical bonds, confirming the adsorption of O intermediates on S.<sup>65</sup> These XPS results are consistent with our DFT calculations and *operando* FTIR results, further establishing the C–S region in thienothiophene as the active catalytic center for oxygen redox reactions. The poststability XRD and TEM measurement also confirmed the COF shells' crystal structure could be well retained, suggesting that TAPTt COF has good electrochemical stability (Figure S31).

## CONCLUSIONS

In summary, we report a metal-free and carbon-based coaxial 1D vdWH, which has a CNT core and TAPTt-COF shells with a tunable thickness from 2 to 4 nm. At the COF shell thickness of 3 nm, the optimal CC-3 vdWH can catalyze the OER *via* the 4e<sup>-</sup> pathway to deliver a TOF of 0.134 s<sup>-1</sup> at an overpotential of 400 mV. The small potential difference between ORR  $E_{1/2}$  and OER  $\eta_{10}$  of 791 mV outperforms most recently reported metal-free bifunctional oxygen electrocatalysts. It enables high-performance rechargeable ZABs with a large specific capacity of 696 mAh g<sub>zn</sub><sup>-1</sup> ( $j = 40$  mA cm<sup>-2</sup>) and excellent cycling stability. Using DFT calculations, UV-vis DRS, and UPS analysis, we show that the strong n-type electronic interaction between CNTs and COF shells is the origin of the significantly improved catalytic activity. Further, we provide a quantitative explanation of the COF shell thickness-dependent catalytic activity by the carrier decay model, providing mechanistic insights into the function of such heterostructured catalysts. The well-defined chemical structure further pinpoints the C–S region on the thienothiophene moiety of TAPTt COF as the active catalytic center through our theoretical calculations, experimental *operando* FTIR, and *ex situ* XPS studies. Our synthesis strategy demonstrated here affords an alternative approach to design and synthesize various multidimensional vdWHs for exploring fundamental physics and chemistry, as

well as practical applications in electrochemistry, electronics, photonics, and beyond.

## METHODS

**Material Synthesis.** MWCNTs (FT9000, CNano, 10–25 nm in diameter) were first purified by a 2 h thermal treatment at 300 °C in airflow, followed by refluxing in 3 M HCl for 6 h to remove amorphous carbon and metal residues. Purified CNTs were washed with deionized water and then dried in a vacuum oven. Afterward, CNTs were thermally annealed in Ar flow (99.999%, BOC) at 1000 °C for 2 h to remove surface functional groups, and then dispersed in DMAc by bath sonication at a concentration of 5 mg mL<sup>-1</sup>. TTAP and TtDCA were dissolved in 5 mL of CNT dispersion at a molar ratio of 1:2. Assuming the production yield of COF at around 80%, the quantities of TTAP and TtDCA were adjusted to yield CC-X 1D vdWHs with different weight ratios between CNTs and COF precursors ( $m_{\text{CNTs}}/m_{\text{precursors}} = 1, 2, \text{ and } 4$ ). The mixtures were frozen and thawed for three cycles before adding 10  $\mu\text{L}$  of 6 M aqueous acetic acid solution and flame sealed. The solvothermal reaction took place at 120 °C and remained under stirred for 3 days. After cooling to room temperature, the solid products were recovered by filtration and repeatedly washed with pure DMAc before dried under vacuum. The reference CC-P sample was prepared by physically mixing TAPt-COF and CNTs at a mass ratio of 1:2. The mixture was ground in an agate mortar for 30 min and then dissolved in 2-propanol. The solvent was evaporated after bath sonication for 60 min.

**Characterization.** The FTIR spectra were collected on an FTIR spectrometer (Nicolet 6700, Thermo Scientific) in the attenuated total reflection mode. The *operando* tests were performed on the same FTIR spectrometer with an *in situ* electrochemical cell (PIKE Technologies). The ssNMR spectra were collected on an NMR spectrometer (Avance III, Bruker). N<sub>2</sub> physisorption isotherms were recorded on a gas adsorption analyzer (iQ2, Quantachrome) at 77 K. XRD patterns were collected on an XRD diffractometer (X'Pert, PANalytical) with a Cu K $\alpha$  X-ray source. Electron microscope images were taken on a SEM (Ultra Plus, Zeiss) and a TEM (JEM-2200, JEOL) under an acceleration voltage of 80 kV. UV–vis DRS measurement was tested on a UV spectrometer (UV-3600, Shimadzu) using BaSO<sub>4</sub> for background correction. XPS and UPS spectra were collected on an XPS spectrometer (K-Alpha+, Thermo Scientific) equipped with an Al K $\alpha$  (1486.3 eV) and a He discharge lamp (21.2 eV). All binding energies were corrected with graphite. Mott–Schottky plots were developed by using the capacitance obtained from EIS measurement performed at various potentials in an Ar saturated 0.1 M KOH electrolyte.

**Electrocatalyst Performance Tests.** Electrocatalysts' electrochemical performance was evaluated using an electrochemical workstation (760E, CHI) using the three-electrode configuration in 0.1 M KOH electrolyte at 25 °C. A Pt mesh, and a precalibrated Hg/HgO electrode (0.1 M NaOH) served as the counter and the reference electrodes, respectively. All potentials reported were corrected to a RHE by  $0.165 + 0.0591 \times \text{pH}$ . Electrocatalysts were dispersed in water/2-propanol (v/v:1/9) solution by bath sonication to reach a concentration of 5 mg mL<sup>-1</sup>. The working electrode was prepared by loading 0.2 mg cm<sup>-2</sup> of electrocatalysts on a prepolished rotary ring-disk electrode (RRDE, E6R2, Pine Instrument, glassy carbon disk with an outer diameter of 5.5 mm, Pt ring with an inner diameter of 6.5 mm and an outer diameter of 8.5 mm) with a calibrated collection efficiency ( $N$ ) is 0.379. The electrocatalyst was precycled by 20 CV scans between 0.1–1 V<sub>RHE</sub> for ORR or 1.2–1.8 V<sub>RHE</sub> for OER in Ar saturated 0.1 M KOH electrode. Afterward, LSV curves were obtained in O<sub>2</sub> saturated 0.1 M KOH electrolyte at a scan rate of 2 mV s<sup>-1</sup> without iR-compensation.

For ORR tests, commercial Pt/C (20 wt %, on Vulcan-XC-72R, Sigma) was tested under identical loading as the references. Selectivity toward H<sub>2</sub>O<sub>2</sub> formation ( $H_2O_2\%$ ) and the ORR electron transfer number ( $n$ ) were calculated from experimental data obtained using RRDEs in O<sub>2</sub> saturated electrolytes by eq 1 and (2), respectively

$$H_2O_2\% = 200 \times \frac{i_{\text{ring}}/N}{i_{\text{disk}} + i_{\text{ring}}/N} \quad (1)$$

$$n = 4 \times \frac{i_{\text{disk}}}{i_{\text{disk}} + i_{\text{ring}}/N} \quad (2)$$

where  $i_{\text{ring}}$  and  $i_{\text{disk}}$  are the currents obtained from the Pt ring and GC disk, respectively.  $N$  is the calibrated collection efficiency. The electron transfer number ( $n$ ) and  $j_k$  were also calculated using the K–L equation

$$1/j = 1/j_L + 1/j_K = 1/B\omega^{1/2} + 1/j_K \quad (3)$$

$$B = 0.62nFC_0(D_0)^{2/3}\nu^{-1/6} \quad (4)$$

$$j_K = nFkC_0 \quad (5)$$

where  $j$  is the measured current density,  $j_k$  and  $j_L$  are the kinetic- and diffusion-limiting current densities,  $\omega$  is the angular velocity,  $n$  is the transferred electron number,  $F$  is the Faraday constant (96485 C mol<sup>-1</sup>),  $C_0$  is the saturated concentration of O<sub>2</sub> in 0.1 M KOH at room temperature,  $D_0$  is diffusion coefficient of oxygen,  $\nu$  is the kinematic viscosity of the electrolyte at room temperature, and  $k$  is the electron-transfer rate constant.

For OER tests, the Faradaic efficiency was assessed on an RRDE in Ar saturated 0.1 M KOH electrolytes. The Pt ring was biased at 0.4 V<sub>RHE</sub>, and the GC disk was biased at 1.5 V<sub>RHE</sub>. The H<sub>2</sub>O<sub>2</sub> selectivity was calculated by eq 1 to determine the catalyst efficiency toward the 4-electron OER. The OER TOF of electrocatalysts was calculated by assuming all S–C regions in COF shells are active sites, using eq 6 shown below

$$\text{TOF} = \frac{i}{4 \times 96485 \times n} \quad (6)$$

where  $i$  is the current and  $n$  is the number of active sites, which is calculated by eq 7

$$n = \frac{2 \times m \times w}{M_w} \quad (7)$$

where  $m$  is the mass of electrocatalysts loaded on the electrode,  $w$  is the mass fraction of COF in electrocatalysts, and  $M_w$  is the molecular weight of a single unit of TAPt-COF (~370 g mol<sup>-1</sup>), containing two identical C–S regions. The electrodes for the water electrolyzer were prepared by coating 0.2 mg cm<sup>-2</sup> electrocatalysts on carbon clothes with a geometric dimension of 1 cm<sup>2</sup>.

**Computational Method.** DFT calculations in this study were performed using the VASP code. Electron correlation was calculated using the generalized gradient approximation method with the functional developed by Perdew, Burke, and Ernzerhof. Core electrons were considered using the projector augmented wave method.<sup>66,67</sup> The valence electrons were described by expanding the Kohn–Sham wave functions in a plane-wave basis set, with a kinetic cutoff of 400 eV.<sup>68</sup> Convergence was established when the forces of each atom were lower than 0.05 eV Å<sup>-1</sup>. A  $\gamma$ -point sampling was used for all calculations. The reaction free energies of ORR were calculated using the computational hydrogen electrode method.<sup>61</sup>

**Zn–Air Battery Tests.** Air electrodes were prepared by depositing electrocatalysts on carbon cloth gas-diffusion layers with a mass loading of 0.5 mg cm<sup>-2</sup>. Reference air electrodes were prepared by depositing commercial Pt/C and IrO<sub>2</sub> catalysts (with a 1/1 molar ratio between Pt/Ir) at the same mass loading. A 6 M KOH solution with 0.2 M ZnCl<sub>2</sub> was used as the electrolyte. The total volume of electrolytes in every cell is about 20 mL. A piece of Zn foil (0.2 mm in thickness, 99.9%, Sigma) was used as the Zn electrode. The battery performance was evaluated in ambient air at ~25 °C using a battery tester (CT2001, Land).

## ASSOCIATED CONTENT

## Supporting Information

The Supporting Information is available free of charge at <https://pubs.acs.org/doi/10.1021/acsnano.0c10242>.

FTIR, ssNMR, XPS spectra, AFM, SEM, and TEM images, XRD patterns, N<sub>2</sub> physisorption isotherms, TGA profiles of TAPTt-COF, MWCNTs, and CC-X vdWHs; ORR LSV curves of Pt/C and CC-X vdWHs; CV curves and calculated C<sub>dl</sub> of CC-X vdWHs; ECSA-normalized OER LSV curves and TOFs of TAPTt-COF, CC-x, and CC-P; activity atlas of various bifunctional carbon electrocatalyst for ORR and OER; performance comparison of recently reported metal-free and carbon-based ORR and OER electrocatalysts; schematic illustration of carrier injection from CNTs to a COF shell; Mott–Schottky plots of TAPTt-COF and CC-x VdWHs; relationship between the reciprocal of the slope in the Mott–Schottky plot as a function of the COF shell thickness; free energy diagram of oxygen reaction intermediates on the most feasible S–C active site; DFT models of ORR intermediates adsorbed on other possible sites on TAPTt COF; open circuit potential vs time of ZABs assembled using CC-3 and Pt–Ir/C catalysts; XPS spectra, XRD patterns, and a TEM image of CC-3 after the ZAB cycling test (PDF)

## AUTHOR INFORMATION

## Corresponding Authors

**Graeme Henkelman** – Department of Chemistry and the Oden Institute for Computational and Engineering Sciences, The University of Texas at Austin, Austin, Texas 78712, United States; [orcid.org/0000-0002-0336-7153](https://orcid.org/0000-0002-0336-7153); Email: [henkelman@utexas.edu](mailto:henkelman@utexas.edu)

**Li Wei** – School of Chemical and Biomolecular Engineering, The University of Sydney, Darlington 2006, NSW, Australia; [orcid.org/0000-0001-8771-2921](https://orcid.org/0000-0001-8771-2921); Email: [lwei@sydney.edu.au](mailto:lwei@sydney.edu.au)

**Yuan Chen** – School of Chemical and Biomolecular Engineering, The University of Sydney, Darlington 2006, NSW, Australia; [orcid.org/0000-0001-9059-3839](https://orcid.org/0000-0001-9059-3839); Email: [yuan.chen@sydney.edu.au](mailto:yuan.chen@sydney.edu.au)

## Authors

**Chang Liu** – School of Chemical and Biomolecular Engineering, The University of Sydney, Darlington 2006, NSW, Australia

**Fei Liu** – State Key Laboratory of Applied Microbiology Southern China, Guangdong Provincial Key Laboratory of Microbial Culture Collection and Application, Guangdong Institute of Microbiology, Guangzhou 510070, Guangdong, China

**Hao Li** – Department of Chemistry and the Oden Institute for Computational and Engineering Sciences, The University of Texas at Austin, Austin, Texas 78712, United States; [orcid.org/0000-0002-7577-1366](https://orcid.org/0000-0002-7577-1366)

**Junsheng Chen** – School of Chemical and Biomolecular Engineering, The University of Sydney, Darlington 2006, NSW, Australia

**Jingyuan Fei** – School of Chemical and Biomolecular Engineering, The University of Sydney, Darlington 2006, NSW, Australia

**Zixun Yu** – School of Chemical and Biomolecular Engineering, The University of Sydney, Darlington 2006, NSW, Australia

**Ziwen Yuan** – School of Chemical and Biomolecular Engineering, The University of Sydney, Darlington 2006, NSW, Australia; [orcid.org/0000-0002-3331-0668](https://orcid.org/0000-0002-3331-0668)

**Chaojun Wang** – School of Chemical and Biomolecular Engineering, The University of Sydney, Darlington 2006, NSW, Australia

**Huilong Zheng** – Department of Chemistry and the Oden Institute for Computational and Engineering Sciences, The University of Texas at Austin, Austin, Texas 78712, United States; [orcid.org/0000-0001-8347-3724](https://orcid.org/0000-0001-8347-3724)

**Zongwen Liu** – School of Chemical and Biomolecular Engineering, The University of Sydney, Darlington 2006, NSW, Australia

**Meiyong Xu** – State Key Laboratory of Applied Microbiology Southern China, Guangdong Provincial Key Laboratory of Microbial Culture Collection and Application, Guangdong Institute of Microbiology, Guangzhou 510070, Guangdong, China; [orcid.org/0000-0001-7276-4219](https://orcid.org/0000-0001-7276-4219)

Complete contact information is available at: <https://pubs.acs.org/doi/10.1021/acsnano.0c10242>

## Author Contributions

<sup>†</sup>C.L., F.L., and H.L. contributed equally.

## Notes

The authors declare no competing financial interest.

## ACKNOWLEDGMENTS

We thank funding support from the Australian Research Council under the Future Fellowships scheme (FT160100107) and Discovery Programme (DP180102210), support from GDAS' Special Project of Science and Technology Development (2019GDASYL-0104005 and 2020GDASYL-20200402001). H.L. and G.H. acknowledge the Welch Foundation (F-1841) and the Texas Advanced Computing Center for computational resources.

## REFERENCES

- (1) Zhao, X.; Pachfule, P.; Li, S.; Langenhahn, T.; Ye, M.; Schlesiger, C.; Praetz, S.; Schmidt, J.; Thomas, A. Macro/Microporous Covalent Organic Frameworks for Efficient Electrocatalysis. *J. Am. Chem. Soc.* **2019**, *141* (16), 6623–6630.
- (2) Guo, J.; Lin, C. Y.; Xia, Z.; Xiang, Z. A Pyrolysis-Free Covalent Organic Polymer for Oxygen Reduction. *Angew. Chem., Int. Ed.* **2018**, *57* (38), 12567–12572.
- (3) Yang, S.; Yu, Y.; Dou, M.; Zhang, Z.; Dai, L.; Wang, F. Two-Dimensional Conjugated Aromatic Networks as High-Site-Density and Single-Atom Electrocatalysts for the Oxygen Reduction Reaction. *Angew. Chem., Int. Ed.* **2019**, *58* (41), 14724–14730.
- (4) Peng, P.; Shi, L.; Huo, F.; Mi, C.; Wu, X.; Zhang, S.; Xiang, Z. A Pyrolysis-Free Path toward Superiorly Catalytic Nitrogen-Coordinated Single Atom. *Sci. Adv.* **2019**, *5* (8), No. eaaw2322.
- (5) Li, B. Q.; Zhang, S. Y.; Wang, B.; Xia, Z. J.; Tang, C.; Zhang, Q. A Porphyrin Covalent Organic Framework Cathode for Flexible Zn-Air Batteries. *Energy Environ. Sci.* **2018**, *11* (7), 1723–1729.
- (6) Peng, P.; Zhou, Z.; Guo, J.; Xiang, Z. Well-Defined 2D Covalent Organic Polymers for Energy Electrocatalysis. *ACS Energy Lett.* **2017**, *2* (6), 1308–1314.
- (7) Feng, X.; Ding, X.; Jiang, D. Covalent Organic Frameworks. *Chem. Soc. Rev.* **2012**, *41* (18), 6010–6022.
- (8) Ding, S. Y.; Wang, W. Covalent Organic Frameworks (COFs): From Design to Applications. *Chem. Soc. Rev.* **2013**, *42* (2), 548–68.

- (9) Cui, X.; Lei, S.; Wang, A. C.; Gao, L.; Zhang, Q.; Yang, Y.; Lin, Z. Emerging Covalent Organic Frameworks Tailored Materials for Electrocatalysis. *Nano Energy* **2020**, *70*, 104525.
- (10) Yang, D. J.; Zhang, L. J.; Yan, X. C.; Yao, X. D. Recent Progress in Oxygen Electrocatalysts for Zinc-Air Batteries. *Small Methods* **2017**, *1* (12), 1700209.
- (11) Chen, X.; Zhou, Z.; Karahan, H. E.; Shao, Q.; Wei, L.; Chen, Y. Recent Advances in Materials and Design of Electrochemically Rechargeable Zinc-Air Batteries. *Small* **2018**, *14* (44), No. 1801929.
- (12) Lu, Z.; Wang, J.; Huang, S.; Hou, Y.; Li, Y.; Zhao, Y.; Mu, S.; Zhang, J.; Zhao, Y. N,B-Codoped Defect-Rich Graphitic Carbon Nanocages as High Performance Multifunctional Electrocatalysts. *Nano Energy* **2017**, *42*, 334–340.
- (13) Fu, J.; Cano, Z. P.; Park, M. G.; Yu, A.; Fowler, M.; Chen, Z. Electrically Rechargeable Zinc-Air Batteries: Progress, Challenges, and Perspectives. *Adv. Mater.* **2017**, *29* (7), 1604685.
- (14) Pan, Z. F.; An, L.; Zhao, T. S.; Tang, Z. K. Advances and Challenges in Alkaline Anion Exchange Membrane Fuel Cells. *Prog. Energy Combust. Sci.* **2018**, *66*, 141–175.
- (15) Du, H.; Zhao, C. X.; Lin, J.; Guo, J.; Wang, B.; Hu, Z.; Shao, Q.; Pan, D.; Wujcik, E. K.; Guo, Z. Carbon Nanomaterials in Direct Liquid Fuel Cells. *Chem. Rec.* **2018**, *18* (9), 1365–1372.
- (16) Qi, J.; Zhang, W.; Cao, R. Solar-to-Hydrogen Energy Conversion Based on Water Splitting. *Adv. Energy Mater.* **2018**, *8* (5), 1701620.
- (17) Vincent, I.; Bessarabov, D. Low Cost Hydrogen Production by Anion Exchange Membrane Electrolysis: A Review. *Renewable Sustainable Energy Rev.* **2018**, *81*, 1690–1704.
- (18) Mondal, S.; Mohanty, B.; Nurhuda, M.; Dalapati, S.; Jana, R.; Addicoat, M.; Datta, A.; Jena, B. K.; Bhaumik, A. A Thiadiazole-Based Covalent Organic Framework: A Metal-Free Electrocatalyst toward Oxygen Evolution Reaction. *ACS Catal.* **2020**, *10* (10), 5623–5630.
- (19) Patra, B. C.; Khilari, S.; Manna, R. N.; Mondal, S.; Pradhan, D.; Pradhan, A.; Bhaumik, A. A Metal-Free Covalent Organic Polymer for Electrocatalytic Hydrogen Evolution. *ACS Catal.* **2017**, *7* (9), 6120–6127.
- (20) Li, X.; Gao, Q.; Aneesh, J.; Xu, H. S.; Chen, Z. X.; Tang, W.; Liu, C. B.; Shi, X. Y.; Adarsh, K. V.; Lu, Y. X.; Loh, K. P. Molecular Engineering of Bandgaps in Covalent Organic Frameworks. *Chem. Mater.* **2018**, *30* (16), 5743–5749.
- (21) Jin, E.; Asada, M.; Xu, Q.; Dalapati, S.; Addicoat, M. A.; Brady, M. A.; Xu, H.; Nakamura, T.; Heine, T.; Chen, Q. Two-Dimensional  $sp^2$  Carbon-Conjugated Covalent Organic Frameworks. *Science* **2017**, *357* (6352), 673–676.
- (22) Chen, X.; Zhang, H.; Ci, C.; Sun, W.; Wang, Y. Few-Layered Boronic Ester Based Covalent Organic Frameworks/Carbon Nanotube Composites for High-Performance K-Organic Batteries. *ACS Nano* **2019**, *13* (3), 3600–3607.
- (23) Sun, B.; Liu, J.; Cao, A.; Song, W.; Wang, D. Interfacial Synthesis of Ordered and Stable Covalent Organic Frameworks on Amino-Functionalized Carbon Nanotubes with Enhanced Electrochemical Performance. *Chem. Commun.* **2017**, *53* (47), 6303–6306.
- (24) Gomes, R.; Bhattacharyya, A. J. Carbon Nanotube-Templated Covalent Organic Framework Nanosheets as an Efficient Sulfur Host for Room-Temperature Metal-Sulfur Batteries. *ACS Sustainable Chem. Eng.* **2020**, *8* (15), 5946–5953.
- (25) Wang, L.; Xie, Y.; Yang, Y.; Liang, H.; Wang, L.; Song, Y. Electroactive Covalent Organic Frameworks/Carbon Nanotubes Composites for Electrochemical Sensing. *ACS Appl. Nano Mater.* **2020**, *3* (2), 1412–1419.
- (26) Sun, Y.; Waterhouse, G. I.; Xu, L.; Qiao, X.; Xu, Z. Three-Dimensional Electrochemical Sensor with Covalent Organic Framework Decorated Carbon Nanotubes Signal Amplification for the Detection of Furozolidone. *Sens. Actuators, B* **2020**, *321*, 128501.
- (27) Liang, J.; Zheng, Y.; Chen, J.; Liu, J.; Hulicova-Jurcakova, D.; Jaroniec, M.; Qiao, S. Z. Facile Oxygen Reduction on a Three-Dimensionally Ordered Macroporous Graphitic  $C_3N_4$ /Carbon Composite Electrocatalyst. *Angew. Chem., Int. Ed.* **2012**, *51* (16), 3892–6.
- (28) Zheng, Y.; Jiao, Y.; Zhu, Y.; Li, L. H.; Han, Y.; Chen, Y.; Du, A.; Jaroniec, M.; Qiao, S. Z. Hydrogen Evolution by a Metal-Free Electrocatalyst. *Nat. Commun.* **2014**, *5*, 3783.
- (29) Tian, G. L.; Zhao, M. Q.; Yu, D.; Kong, X. Y.; Huang, J. Q.; Zhang, Q.; Wei, F. Nitrogen-Doped Graphene/Carbon Nanotube Hybrids: *In Situ* Formation on Bifunctional Catalysts and Their Superior Electrocatalytic Activity for Oxygen Evolution/Reduction Reaction. *Small* **2014**, *10* (11), 2251–9.
- (30) Chen, S.; Duan, J.; Jaroniec, M.; Qiao, S.-Z. Nitrogen and Oxygen Dual-Doped Carbon Hydrogel Film as a Substrate-Free Electrode for Highly Efficient Oxygen Evolution Reaction. *Adv. Mater.* **2014**, *26* (18), 2925–2930.
- (31) Niu, W. H.; Marcus, K.; Zhou, L.; Li, Z.; Shi, L.; Liang, K.; Yang, Y. Enhancing Electron Transfer and Electrocatalytic Activity on Crystalline Carbon-Conjugated  $g-C_3N_4$ . *ACS Catal.* **2018**, *8* (3), 1926–1931.
- (32) Gao, R.; Dai, Q.; Du, F.; Yan, D.; Dai, L.  $C_{60}$ -Adsorbed Single-Walled Carbon Nanotubes as Metal-Free, pH-Universal, and Multifunctional Catalysts for Oxygen Reduction, Oxygen Evolution, and Hydrogen Evolution. *J. Am. Chem. Soc.* **2019**, *141* (29), 11658–11666.
- (33) Wang, S.; Yu, D.; Dai, L. Polyelectrolyte Functionalized Carbon Nanotubes as Efficient Metal-Free Electrocatalysts for Oxygen Reduction. *J. Am. Chem. Soc.* **2011**, *133* (14), 5182–5.
- (34) Hu, Q.; Li, G.; Liu, X.; Zhu, B.; Chai, X.; Zhang, Q.; Liu, J.; He, C. Superhydrophilic Phytic-Acid-Doped Conductive Hydrogels as Metal-Free and Binder-Free Electrocatalysts for Efficient Water Oxidation. *Angew. Chem., Int. Ed.* **2019**, *58* (13), 4318–4322.
- (35) Jariwala, D.; Marks, T. J.; Hersam, M. C. Mixed-Dimensional van der Waals Heterostructures. *Nat. Mater.* **2017**, *16* (2), 170–181.
- (36) Liu, Y.; Weiss, N. O.; Duan, X. D.; Cheng, H. C.; Huang, Y.; Duan, X. F. van der Waals Heterostructures and Devices. *Nat. Rev. Mater.* **2016**, *1* (9), 16042.
- (37) Xiang, R.; Inoue, T.; Zheng, Y.; Kumamoto, A.; Qian, Y.; Sato, Y.; Liu, M.; Tang, D.; Gokhale, D.; Guo, J.; Hisama, K.; Yotsumoto, S.; Ogamoto, T.; Arai, H.; Kobayashi, Y.; Zhang, H.; Hou, B.; Anisimov, A.; Maruyama, M.; Miyata, Y.; et al. One-Dimensional van der Waals Heterostructures. *Science* **2020**, *367* (6477), 537–542.
- (38) El-Sawy, A. M.; Mosa, I. M.; Su, D.; Guild, C. J.; Khalid, S.; Joesten, R.; Rusling, J. F.; Suib, S. L. Controlling the Active Sites of Sulfur-Doped Carbon Nanotube-Graphene Nanolobes for Highly Efficient Oxygen Evolution and Reduction Catalysis. *Adv. Energy Mater.* **2016**, *6* (5), 1501966.
- (39) Nakashima, N.; Tomonari, Y.; Murakami, H. Water-Soluble Single-Walled Carbon Nanotubes *via* Noncovalent Sidewall-Functionalization with a Pyrene-Carrying Ammonium Ion. *Chem. Lett.* **2002**, *31* (6), 638–639.
- (40) Lu, X.; Yim, W.-L.; Suryanto, B. H. R.; Zhao, C. Electrocatalytic Oxygen Evolution at Surface-Oxidized Multiwall Carbon Nanotubes. *J. Am. Chem. Soc.* **2015**, *137* (8), 2901–7.
- (41) Liu, H.; Chu, J.; Yin, Z.; Cai, X.; Zhuang, L.; Deng, H. Covalent Organic Frameworks Linked by Amine Bonding for Concerted Electrochemical Reduction of  $CO_2$ . *Chem.* **2018**, *4* (7), 1696–1709.
- (42) Suntivich, J.; May, K. J.; Gasteiger, H. A.; Goodenough, J. B.; Shao-Horn, Y. A Perovskite Oxide Optimized for Oxygen Evolution Catalysis from Molecular Orbital Principles. *Science* **2011**, *334* (6061), 1383–1385.
- (43) Li, Q.; He, T.; Zhang, Y.-Q.; Wu, H.; Liu, J.; Qi, Y.; Lei, Y.; Chen, H.; Sun, Z.; Peng, C.; Yi, L.; Zhang, Y. Biomass Waste-Derived 3D Metal-Free Porous Carbon as a Bifunctional Electrocatalyst for Rechargeable Zinc-Air Batteries. *ACS Sustainable Chem. Eng.* **2019**, *7* (20), 17039–17046.
- (44) Liu, Q.; Wang, Y. B.; Dai, L. M.; Yao, J. N. Scalable Fabrication of Nanoporous Carbon Fiber Films as Bifunctional Catalytic Electrodes for Flexible Zn-Air Batteries. *Adv. Mater.* **2016**, *28* (15), 3000–3006.
- (45) Ma, T. Y.; Ran, J.; Dai, S.; Jaroniec, M.; Qiao, S. Z. Phosphorus-Doped Graphitic Carbon Nitrides Grown *In Situ* on Carbon-Fiber

Paper: Flexible and Reversible Oxygen Electrodes. *Angew. Chem., Int. Ed.* **2015**, *54* (15), 1–6.

(46) Liu, S.; Zhang, H.; Zhao, Q.; Zhang, X.; Liu, R.; Ge, X.; Wang, G.; Zhao, H.; Cai, W. Metal-Organic Framework Derived Nitrogen-Doped Porous Carbon@Graphene Sandwich-Like Structured Composites as Bifunctional Electrocatalysts for Oxygen Reduction and Evolution Reactions. *Carbon* **2016**, *106*, 74–83.

(47) Qian, Y.; Hu, Z.; Ge, X.; Yang, S.; Peng, Y.; Kang, Z.; Liu, Z.; Lee, J. Y.; Zhao, D. A Metal-Free ORR/OER Bifunctional Electrocatalyst Derived from Metal-Organic Frameworks for Rechargeable Zn-Air Batteries. *Carbon* **2017**, *111*, 641–650.

(48) Qu, K.; Zheng, Y.; Dai, S.; Qiao, S. Z. Graphene Oxide-Polydopamine Derived N, S-Codoped Carbon Nanosheets as Superior Bifunctional Electrocatalysts for Oxygen Reduction and Evolution. *Nano Energy* **2016**, *19*, 373–381.

(49) Jia, N.; Weng, Q.; Shi, Y.; Shi, X.; Chen, X.; Chen, P.; An, Z.; Chen, Y. N-Doped Carbon Nanocages: Bifunctional Electrocatalysts for the Oxygen Reduction and Evolution Reactions. *Nano Res.* **2018**, *11* (4), 1905–1916.

(50) Zhang, J.; Zhao, Z.; Xia, Z.; Dai, L. A Metal-Free Bifunctional Electrocatalyst for Oxygen Reduction and Oxygen Evolution Reactions. *Nat. Nanotechnol.* **2015**, *10*, 444.

(51) Yang, H. B.; Miao, J.; Hung, S.-F.; Chen, J.; Tao, H. B.; Wang, X.; Zhang, L.; Chen, R.; Gao, J.; Chen, H. M.; Dai, L.; Liu, B. Identification of Catalytic Sites for Oxygen Reduction and Oxygen Evolution in N-Doped Graphene Materials: Development of Highly Efficient Metal-Free Bifunctional Electrocatalyst. *Sci. Adv.* **2016**, *2* (4), e1501122.

(52) Lin, X.; Peng, P.; Guo, J.; Xiang, Z. Reaction Milling for Scalable Synthesis of N, P-Codoped Covalent Organic Polymers for Metal-Free Bifunctional Electrocatalysts. *Chem. Eng. J.* **2019**, *358*, 427–434.

(53) Guo, Y.; Yao, S.; Gao, L.; Chen, A.; Jiao, M.; Cui, H.; Zhou, Z. Boosting Bifunctional Electrocatalytic Activity in S and N Co-Doped Carbon Nanosheets for High-Efficiency Zn-Air Batteries. *J. Mater. Chem. A* **2020**, *8* (8), 4386–4395.

(54) Wang, H.-F.; Tang, C.; Zhang, Q. Template Growth of Nitrogen-Doped Mesoporous Graphene on Metal Oxides and Its Use as a Metal-Free Bifunctional Electrocatalyst for Oxygen Reduction and Evolution Reactions. *Catal. Today* **2018**, *301*, 25–31.

(55) Xiao, X.; Li, X.; Wang, Z.; Yan, G.; Guo, H.; Hu, Q.; Li, L.; Liu, Y.; Wang, J. Robust Template-Activator Cooperated Pyrolysis Enabling Hierarchically Porous Honeycombed Defective Carbon as Highly-Efficient Metal-Free Bifunctional Electrocatalyst for Zn-Air Batteries. *Appl. Catal., B* **2020**, *265*, 118603.

(56) Wang, Z.; Yang, B.; Wang, Y.; Zhao, Y.; Cao, X. M.; Hu, P. Identifying the Trend of Reactivity for  $sp^2$  Materials: An Electron Delocalization Model from First Principles Calculations. *Phys. Chem. Chem. Phys.* **2013**, *15* (24), 9498–9502.

(57) Sze, S. M.; Ng, K. K., Physics and Properties of Semiconductors—A Review. *Physics of Semiconductor Devices*, 3rd ed.; John Wiley & Sons: Hoboken, NJ, 2007; pp 5–75.

(58) Cardon, F.; Gomes, W. P. On the Determination of the Flat-Band Potential of a Semiconductor in Contact with a Metal or an Electrolyte from the Mott-Schottky Plot. *J. Phys. D: Appl. Phys.* **1978**, *11* (4), L63–L67.

(59) Hermann, J.; Alfè, D.; Tkatchenko, A. Nanoscale  $\pi$ - $\pi$  Stacked Molecules Are Bound by Collective Charge Fluctuations. *Nat. Commun.* **2017**, *8* (1), 14052.

(60) Cheon, J. Y.; Kim, J. H.; Kim, J. H.; Goddeti, K. C.; Park, J. Y.; Joo, S. H. Intrinsic Relationship between Enhanced Oxygen Reduction Reaction Activity and Nanoscale Work Function of Doped Carbons. *J. Am. Chem. Soc.* **2014**, *136* (25), 8875–8878.

(61) Nørskov, J. K.; Rossmeisl, J.; Logadottir, A.; Lindqvist, L.; Kitchin, J. R.; Bligaard, T.; Jónsson, H. Origin of the Overpotential for Oxygen Reduction at a Fuel-Cell Cathode. *J. Phys. Chem. B* **2004**, *108* (46), 17886–17892.

(62) Gauthier, J. A.; Dickens, C. F.; Chen, L. D.; Doyle, A. D.; Nørskov, J. K. Solvation Effects for Oxygen Evolution Reaction

Catalysis on IrO<sub>2</sub> (110). *J. Phys. Chem. C* **2017**, *121* (21), 11455–11463.

(63) Vacque, V.; Sombret, B.; Huvenne, J. P.; Legrand, P.; Suc, S. Characterisation of the O-O Peroxide Bond by Vibrational Spectroscopy. *Spectrochim. Acta, Part A* **1997**, *53* (1), 55–66.

(64) Noguchi, T.; Nojiri, M.; Takei, K.-i.; Odaka, M.; Kamiya, N. Protonation Structures of Cys-Sulfinic and Cys-Sulfenic Acids in the Photosensitive Nitrile Hydratase Revealed by Fourier Transform Infrared Spectroscopy. *Biochemistry* **2003**, *42* (40), 11642–11650.

(65) Beamson, G.; Briggs, D. *High Resolution XPS of Organic Polymers: The Scienta ESCA300 Database*, 1st ed.; Wiley, 1992.

(66) Hammer, B.; Hansen, L. B.; Nørskov, J. K. Improved Adsorption Energetics within Density-Functional Theory Using Revised Perdew-Burke-Ernzerhof Functionals. *Phys. Rev. B: Condens. Matter Mater. Phys.* **1999**, *59* (11), 7413–7421.

(67) Perdew, J. P.; Burke, K.; Ernzerhof, M. Generalized Gradient Approximation Made Simple. *Phys. Rev. Lett.* **1996**, *77* (18), 3865–3868.

(68) Kohn, W.; Sham, L. J. Self-Consistent Equations Including Exchange and Correlation Effects. *Phys. Rev.* **1965**, *140* (4A), A1133–A1138.